International Journal of Mechanical Sciences 163 (2019) 105131

Contents lists available at ScienceDirect

International Journal of Mechanical Sciences

journal homepage: www.elsevier.com/locate/ijmecsci

Quantifying the anisotropic linear elastic behavior of solids

Yue Mei [a,b,c], Sevan Goenezen [c,*]

[a] State Key Laboratory of Structural Analysis for Industrial Equipment, Department of Engineering Mechanics, Dalian University of Technology, Dalian 116023, China
[b] International Research Center for Computational Mechanics, Dalian University of Technology, China
[c] Department of Mechanical Engineering, Texas A&M University, College Station, TX 77843, USA

ARTICLE INFO

Keywords:
Mechanical testing of heterogeneous materials
Inverse problems
Anisotropy
Composite materials

ABSTRACT

In this work, we present a non-destructive approach to characterize the heterogeneous mechanical behavior of anisotropic elastic solids. This approach is based on iterative inverse algorithms using the framework of finite element discretization schemes. We test the proposed approach with several theoretical studies and observe that for a low noise level in measured displacement fields, it is possible to map the anisotropic linear elastic parameter distributions with high accuracy. We also observe that with additional displacement field measurements, the solution to the inverse problem becomes more unique. However, for higher noise levels (3%), the quality of the reconstructions deteriorates for the parameter C_{12} of the orthotropic elasticity tensor. A theoretical analysis is performed and we demonstrate that this may be due to small gradients of the objective function with respect to C_{12}. Overall, the proposed approach has potential to characterize the anisotropic mechanical behavior of polymer based materials or tissues for pathology.

1. Introduction

Understanding the mechanical behavior of materials is crucial not only in traditional engineering fields including civil engineering, mechanical engineering, aerospace engineering, etc., but also in emerging engineering fields, e.g., to analyze the structural integrity of engineered tissues or to analyze the biomechanical behavior of body parts. A wide range of important mechanical testing approaches such as uniaxial testing, biaxial testing, shear testing are generally utilized for this purpose. In mechanical testing, a sample with predefined geometry is subject to controlled loadings, and the testing system records the applied force and the resulting deformation [1]. With the measured force and deformations, the stress-strain relation can be determined, from which the mechanical properties can be inferred [2]. Beyond linear elastic parameters, these may include nonlinear elastic, viscoelastic, plastic, or anisotropic parameters via curve fitting, using an appropriate constitutive model for stiff solids such as alloys [3,4], concretes [5,6], ceramics [7], and biological tissues [8–10].

With the development of imaging techniques, such as ultrasound, magnetic resonance imaging (MRI), optical coherence tomography (OCT), and digital cameras, it has been possible to measure the spatial distribution of the displacement field that can be used to map the nonhomogeneous mechanical property distributions. Ultrasound based techniques measure quasi-static displacements [11–15] and the wave speed [16–18] to infer the elastic modulus or viscoelastic property distributions. MRI is mainly used to measure shear wave speeds from which the storage and loss modulus distributions can be inferred [19–23]. OCT is mainly used on softer materials such as soft tissues with a penetration depth of about 2 mm [24]. It provides quasi-static and dynamic displacements at micrometer length scales [25–29] to infer the elastic modulus or viscoelastic property distribution. Digital camera images can be used to trace displacement fields on the surface of a specimen provided a speckle pattern [30–32]. The mechanical property distributions of flat samples under two-dimensional loading conditions were computed for nonlinear elastic [33] and elasto-viscoplastic [34,35] materials. In a theoretical study, the linear elastic property distribution was also determined for a non-homogeneous and volumetric solid under three dimensional loading conditions [36,37]. This expands the potential use of digital camera imaging to “view” the interior mechanical property distribution of three dimensional solids.

However, only few works are available on identifying the heterogeneous, linear elastic anisotropic parameter of solids from quasi-static displacement fields [38–40]. In [38], the authors reconstructed the nonhomogeneous anisotropic elastic constants of solids by minimizing the discrepancy in the stress fields. In [39], the authors mapped the nonhomogeneous and transversely isotropic linear elastic parameter distribution of synthetic data and of bones in three dimensions by minimizing the discrepancy between measured and computed displacements. Therein the orientation of the material axes was assumed to be known. From those works, it was apparent that it is a much harder task to recover the anisotropic elastic constants as compared to the isotropic elastic

* Corresponding author.
E-mail address: sevangoenezen@gmail.com (S. Goenezen).

https://doi.org/10.1016/j.ijmecsci.2019.105131
Received 18 September 2018; Received in revised form 6 July 2019; Accepted 3 September 2019
Available online 4 September 2019

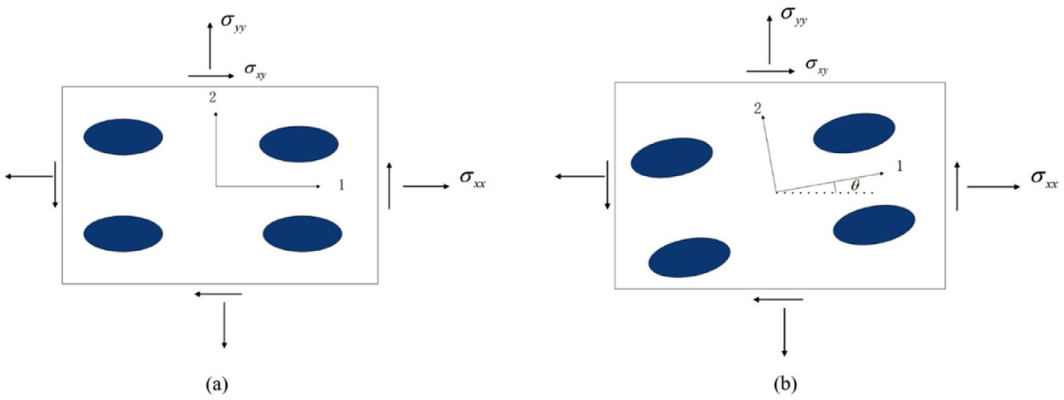

Fig. 1. A schematic diagram of the cross section of a microstructure for an orthotropic material where the elliptic fiber bundles are in dark blue color. (a) The material axes are aligned with the reference axes; (b) the material axes are not aligned with reference axes.

constants. The anisotropic material parameter distribution has been poorly recovered even for low noise levels in measured displacements [38,39]. This is because the number of linear elastic constants for an anisotropic material is significantly higher than that of an isotropic material.

In this work, we solve for the orthotropic linear elastic parameter distributions together with the unknown orientation of material axes that changes as a function of space. In Guchhait et al. [38] the orientation of material axes was introduced as an additional unknown as well, and they utilized a stress formulation in the objective function. In this paper, we minimize the discrepancy between computed and measured displacement fields in the objective function for the orthotropic elastic parameter distribution and material axes orientation. The stability of the solution is controlled with a regularization term. We solve the inverse problem utilizing the adjoint equations to efficiently calculate the gradient of the objective function after discretizing the equations with finite element based schemes. We present the proposed numerical algorithms in Section 2 and evaluate them using three different regularization terms in Section 3. In more detail, we utilize the total variation diminishing regularization in Section 3.1, the L-1 regularization in Section 3.2, and the L-2 regularization in Section 3.3. To understand the outcome of the numerical results, a theoretical analysis will be presented in Section 3.4. In Section 4, we will discuss the numerical results and end with conclusions in Section 5.

2. Methods

2.1. Forward problem formulation for 2-D orthotropic linear elasticity

The strong form can be stated as: Find the displacement $\mathbf{u}$ such that the equilibrium equations are satisfied for prescribed Neumann and Dirichlet boundary conditions and are given by

$$\begin{aligned} \nabla\boldsymbol{\sigma} &= 0 \quad && \text{in } \Omega \\ \mathbf{u} &= \mathbf{g} && \text{on } \Gamma_u \\ \boldsymbol{\sigma}\cdot\mathbf{n} &= \mathbf{t} && \text{on } \Gamma_t \end{aligned} \tag{1}$$

Where $\boldsymbol{\sigma}$ denotes the stress tensor, Ω the problem domain, Γ_u the displacement boundary with prescribed displacements $\mathbf{g}$, and Γ_t the traction boundary with prescribed traction $\mathbf{t}$. Furthermore, we require that $\Gamma_u \cup \Gamma_t = \Omega$, constitutes the entire boundary, and $\Gamma_u \cap \Gamma_t = \emptyset$ yields the empty set.

The constitutive equation here is given for a 2-D orthotropic linear elastic material by:

$$\begin{Bmatrix} \sigma_{xx} \\ \sigma_{yy} \\ \sigma_{xy} \end{Bmatrix} = \begin{bmatrix} C_{11} & C_{12} & 0 \\ C_{12} & C_{22} & 0 \\ 0 & 0 & C_{66} \end{bmatrix} \begin{Bmatrix} \epsilon_{xx} \\ \epsilon_{yy} \\ \gamma_{xy} \end{Bmatrix} \tag{2}$$

where $\gamma_{xy} = 2\epsilon_{xy}$ is the in-plane engineering shear strain. We note that material axes are aligned with the x-y axes as shown in Fig. 1(a). It is noted that there is no coupling effect between shear and axial deformations. In other words, pure shear stresses will only produce pure shear strains, and normal stresses will only result in normal strains. If the material axes are not aligned with the x-y axes, e.g., the material axes are rotated counter-clockwise from the x-y coordinate system by an angle of θ as shown in Fig. 1(b), the stress-strain relation can be rewritten as:

$$\begin{Bmatrix} \sigma_{xx} \\ \sigma_{yy} \\ \sigma_{xy} \end{Bmatrix} = \begin{bmatrix} \tilde{C}_{11} & \tilde{C}_{12} & \tilde{C}_{16} \\ \tilde{C}_{12} & \tilde{C}_{22} & \tilde{C}_{26} \\ \tilde{C}_{16} & \tilde{C}_{26} & \tilde{C}_{66} \end{bmatrix} \begin{Bmatrix} \epsilon_{xx} \\ \epsilon_{yy} \\ \gamma_{xy} \end{Bmatrix} \tag{3}$$

It is noted that the statements we made for the constitutive Eq. (2) do not hold here. The material parameters in Eq. (3) can be expressed in terms of $C_{11}, C_{12}, C_{22}, C_{66}$ and θ, that is,

$$\begin{aligned} \tilde{C}_{11} &= C_{11}\cos^4\theta + C_{22}\sin^4\theta + 2\left(C_{12} + 2C_{66}\right)\sin^2\theta\cos^2\theta \\ \tilde{C}_{22} &= C_{11}\sin^4\theta + C_{22}\cos^4\theta + 2\left(C_{12} + 2C_{66}\right)\sin^2\theta\cos^2\theta \\ \tilde{C}_{12} &= \left(C_{11} + C_{22} - 4C_{66}\right)\sin^2\theta\cos^2\theta + C_{12}\left(\cos^4\theta + \sin^4\theta\right) \\ \tilde{C}_{66} &= \left(C_{11} + C_{22} - 2C_{12} - 2C_{66}\right)\sin^2\theta\cos^2\theta + C_{66}\left(\cos^4\theta + \sin^4\theta\right) \\ \tilde{C}_{16} &= \left(C_{11} - C_{12} - 2C_{66}\right)\sin\theta\cos^3\theta - \left(C_{22} - C_{12} - 2C_{66}\right)\sin^3\theta\cos\theta \\ \tilde{C}_{26} &= \left(C_{11} - C_{12} - 2C_{66}\right)\sin^3\theta\cos\theta - \left(C_{22} - C_{12} - 2C_{66}\right)\sin\theta\cos^3\theta \end{aligned} \tag{4}$$

Eq. (4) is obtained after a coordinate transformation of the stress tensor and strain tensor, as shown in [41]. With the constitutive laws from (3) and (4), the governing equations, and prescribed boundary conditions, we can solve the boundary value problem, also referred to here as the forward problem, for a given problem domain, using finite element methods and determine its displacement fields.

2.2. Inverse problem formulation for 2-D orthotropic linear elasticity

In this paper, we utilize an iterative solution strategy to solve the inverse problem in 2-D for an orthotropic linear elastic material. The inverse problem is stated as: Given N measured displacement fields $\mathbf{u}_1^m, \mathbf{u}_2^m \ldots \mathbf{u}_N^m$, find the material parameter and angle distributions (optimization variables) $\beta = [C_{11}\, C_{12}\, C_{22}\, C_{66}\, \theta]$ such that the objective function

$$F = \frac{1}{2}\sum_{i=1}^{N} \left\| \left(\mathbf{u}_i^c - \mathbf{u}_i^m\right) \right\|_0^2 + \mathrm{Reg}(\beta_i) \tag{5}$$

is minimized. In Eq. (5), $\mathbf{u}_i^c$ is the i th computed displacement field and satisfies the constraint of boundary value problem for the updated mechanical property distributions, obtained at the previous minimization iteration. In Eq. (5), we have omitted the spatial dependencies $\mathbf{x}$ of displacement fields and unknown optimization variables. Further, we note that the discrepancy between computed and measured displacements in Eq. (5) is minimized in the L-2 norm. Additionally, the displacements

and optimization variables are discretized with finite element shape functions, consequently the optimization variables are assumed to be unknowns on finite element mesh nodes. Due to noise in displacement measurements and the ill-posedness of the inverse problem, we augment the objective function in the second term with a regularization term. We employ the total variation diminishing (TVD) regularization [42,43], L-1 regularization, L-2 regularization, and compound regularization (TVD+L-1) [44] given in that order by

$$\begin{aligned}
&\frac{1}{2}\sum_{j=1}^{m}\alpha_j\int_\Omega\sqrt{|\nabla\beta_j|^2+c^2}d\Omega\\
&\frac{1}{2}\sum_{j=1}^{m}\alpha_j\int_\Omega\sqrt{|\beta_j|^2}d\Omega\\
&\frac{1}{2}\sum_{j=1}^{m}\alpha_j\int_\Omega(\beta_j)^2d\Omega\\
&\frac{1}{2}\sum_{j=1}^{m}\alpha_j\int_\Omega\sqrt{|\nabla\beta_j|^2+c^2}d\Omega+\frac{1}{2}\sum_{j=m+1}^{2m}\alpha_j\int_\Omega\sqrt{|\beta_j|^2}d\Omega
\end{aligned}\tag{6}$$

The weight of the regularization term and its contribution to the objective function are controlled by the regularization factor α_j, which is selected by a smoothness criteria discussed in past publications [45,46]. The smoothness criteria leads to a very low standard deviation less than 0.17 in a subregion of the background. In the total variation diminishing regularization, $c=0.01$ is a constant to avoid singularities when computing the gradient of the regularization term.

The constrained optimization problem is solved using a gradient based method, here the L-BFGS method [47,48]. This requires the gradient of the objective function with respect to mechanical properties and angle ($\partial F/\partial\beta_j$) to be computed at every node. To reduce the computational cost in evaluating the gradient, we adopt the adjoint method, which merely requires solving two linear problems at each minimization iteration. In more detail, in the first step we solve the forward problems for each measurement "i" given by the weak form; Find $\mathbf{u}_i^c\in Q$ such that

$$A\left(\mathbf{w}_i,\mathbf{u}_i^c;\beta_j\right)-\int_\Gamma\mathbf{w}_i\cdot\mathbf{t}_i\,d\Gamma=0\qquad\forall\,\mathbf{w}_i\in V\tag{7}$$

where $A(\mathbf{w}_i,\mathbf{u}_i^c;\beta_j)=\int_\Omega\nabla\mathbf{w}_i:\boldsymbol{\sigma}_i\,d\Omega$, the subscript i denotes (no Einstein summation over repeated i here) the i-th measurement, and the stress tensor $\boldsymbol{\sigma}_i$ was defined in Eq. (3) in terms of the strain components related to the computed displacements $\mathbf{u}_i^c$ by $\boldsymbol{\varepsilon}_i=\frac{1}{2}(\nabla\mathbf{u}_i^c+(\nabla\mathbf{u}_i^c)^T)$. Further, we define the function spaces Q and V as

$$Q=\{\mathbf{u}|u_k\in H^1(\Omega);\ u_k=g_k\text{ on }\Gamma_u\}\tag{8}$$

$$V=\{\mathbf{w}|w_k\in H^1(\Omega);\ w_k=0\text{ on }\Gamma_u\}\tag{9}$$

In the second step, the dual problem is solved using the computed displacement field $\mathbf{u}_i^c$ from solving the weak form in the first step. In particular, we solve for the Lagrange multipliers $\bar{\mathbf{w}}_i$ for each measurement i given by

$$A\left(\delta\mathbf{u}_i^c,\bar{\mathbf{w}}_i;\beta_j,\mathbf{u}_i^c\right)=\int\delta\mathbf{u}_i^c\cdot(\mathbf{u}_i^c-\mathbf{u}_i^m)d\Omega\qquad\forall\delta\mathbf{u}_i^c\in V\tag{10}$$

With $\mathbf{u}_i^c$ and $\bar{\mathbf{w}}_i$ we can formulate the gradient of the objective function in Eq. (5) with respect to the mechanical property distributions. To this end, we define variations of a function or the functional derivative as

$$\delta f=D_{\beta_j}f\,\delta\beta_j=\left.\frac{d}{d\varepsilon}\right|_{\varepsilon\to0}f(\beta_j+\varepsilon\,\delta\beta_j)\tag{11}$$

We express the variations in the objective function with respect to the mechanical properties as

$$\delta\pi=\sum_{i=1}^{N}\int_\Omega\nabla\mathbf{w}_i:D_{\beta_j}\boldsymbol{\sigma}_i\,\delta\beta_j d\Omega+D_{\beta_j}\mathrm{Reg}(\beta_i)\,\delta\beta_j\tag{12}$$

Table 1
Target orthotropic linear elastic mechanical parameters as defined in Fig. 3.

	C_{11}(kPa)	C_{12}(kPa)	C_{22}(kPa)	C_{66}(kPa)	$\theta(^o)$
background	40	9	150	14	0
inclusion	200	40	300	42	0

from which the gradient can be directly computed. The derivation of Eq. (12) has been omitted here and can be viewed in detail in [45,49,50]. We note that Eqs. (4) to (12) are provided in continuous form. We discretize all spatially varying variables using finite element based discretization schemes, and more precisely with bilinear elements. The computation of the gradient has been derived and expressed in matrix/vector notation in [19,51] as an alternative representation to the continuous form here.

The nodal optimization variables in β are updated at every minimization call until the relative change in the objective function value or gradients is close to machine precision. We note that for 2-D orthotropic linear elasticity, a large number of unknowns must be determined, thus, the solution to the inverse problem may be harder to solve uniquely. To address this issue, we will solve the inverse problem using multiple full-field displacement fields that are significantly distinct from one another.

2.3. Creating theoretical-synthetic displacement fields

The performance of the iterative inverse strategy to characterize the non-homogeneous orthotropic linear elastic parameters and the angle (orientation of the material axes) will be tested with theoretical data, i.e. synthetic displacements obtained from solving boundary value problems. To represent noise in actual displacement measurements, we add white Gaussian noise to both the displacement fields and traction boundary conditions (same noise level to each). To this end, let us consider a 1 cm × 1 cm square problem domain as shown in the first column of Fig. 3. In this problem domain, a stiff inclusion with a radius of 0.1 cm is embedded in a soft background. The specific mechanical parameters for the background and inclusion are given in Table 1. In this case, the mechanical parameters of the background are taken from the parameters of a healthy human skin [52]. First, we assume that the material axes of both background and inclusion are known and aligned with the reference axes, i.e., $\theta=0$. The problem domain has been meshed with 900 bilinear finite elements having uniform grid spacing. We utilize multiple synthetic full-field displacement "measurements" acquired by solving boundary value problems for verification of our inverse problem implementation solution strategy. The location of measured displacement points coincides with the mesh nodes, and the mesh used to solve the inverse problem remains the same. The traction and displacement boundary conditions are defined in Fig. 2(a) and (b) represent uniaxial tension tests, Fig. 2(c) and (d) represent shear tests, and Fig. 2(e) and (f) represent biaxial tests. The prescribed non-zero tractions are given by $t_x=-3$ kPa, $t_y=3$ kPa, $t_{xy}=1.5$ kPa, $t_x^1=0.3$ kPa, $t_y^1=t_y^2=0.3$ kPa and $t_x^2=-0.3$ kPa.

3. Results

3.1. Reconstructions using total variation diminishing regularization

The results in this section utilize the total variation diminishing regularization, defined in the first row of Eq. (6). This regularization type penalizes variations and oscillations and preserves sharp gradients in the mapped solutions. Fig. 3 represents reconstructions using 4 full-field displacement measurements (from Fig. 2(a) to (d)). The target domain is given in column 1 for the orthotropic elatic parameters C_{11}, C_{12}, C_{22}, C_{66} from row 1 to 4, respectively. Reconstructions in columns 2, 3, and

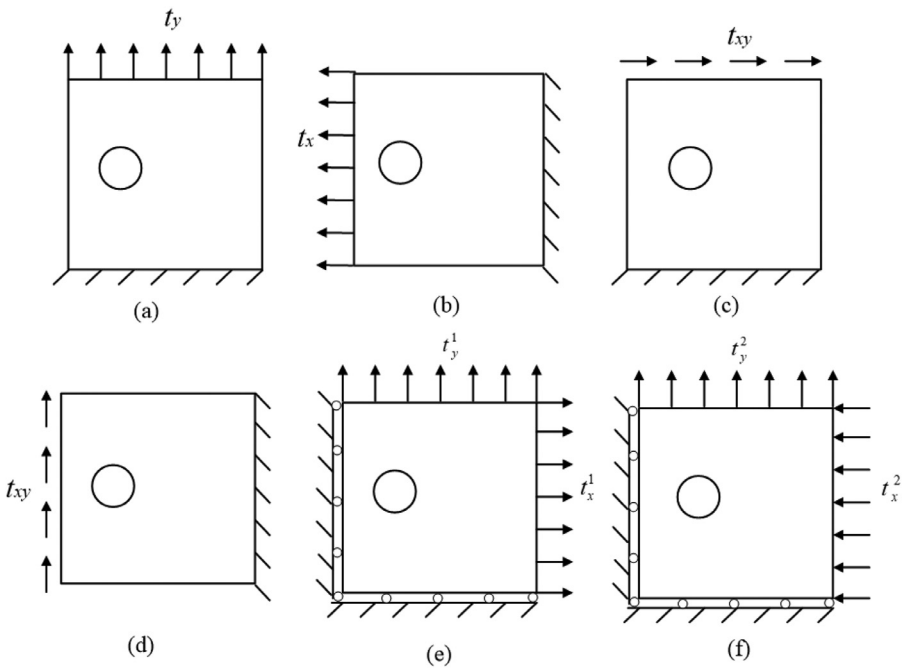

Fig. 2. A total of six prescribed boundary conditions are employed for the problem domain with a stiff inclusion embedded in a soft background to create distinct displacement fields.

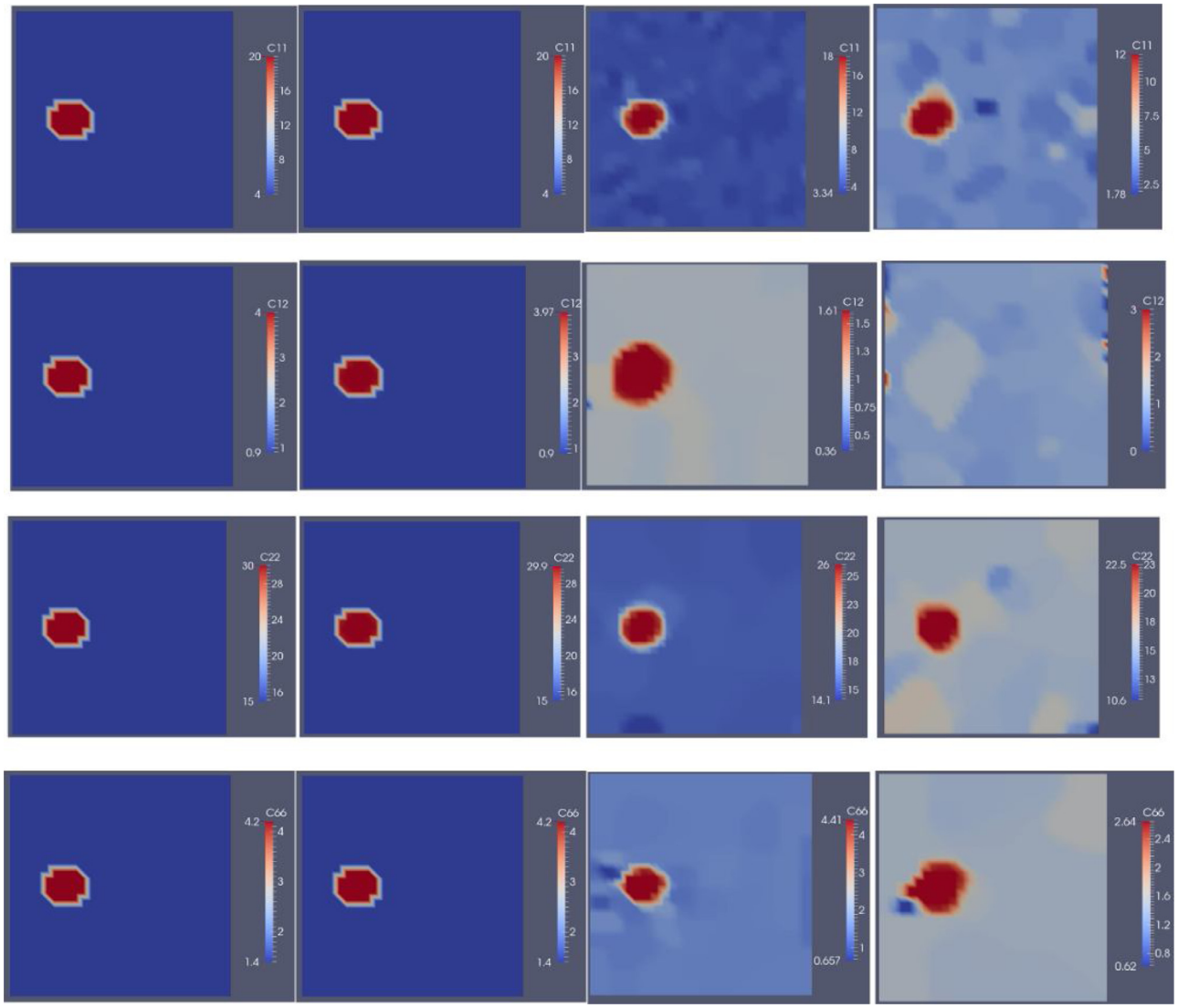

Fig. 3. Problem domain with target material parameter distributions C_{11},C_{12},C_{22},C_{66} are defined in the first column and presented from top row to bottom row, respectively. Column 2 to column 4 represent parameter reconstructions using 4 displacement measurements with 0%, 1%, and 3% noise, respectively. (Unit in the color bar: 10KPa).

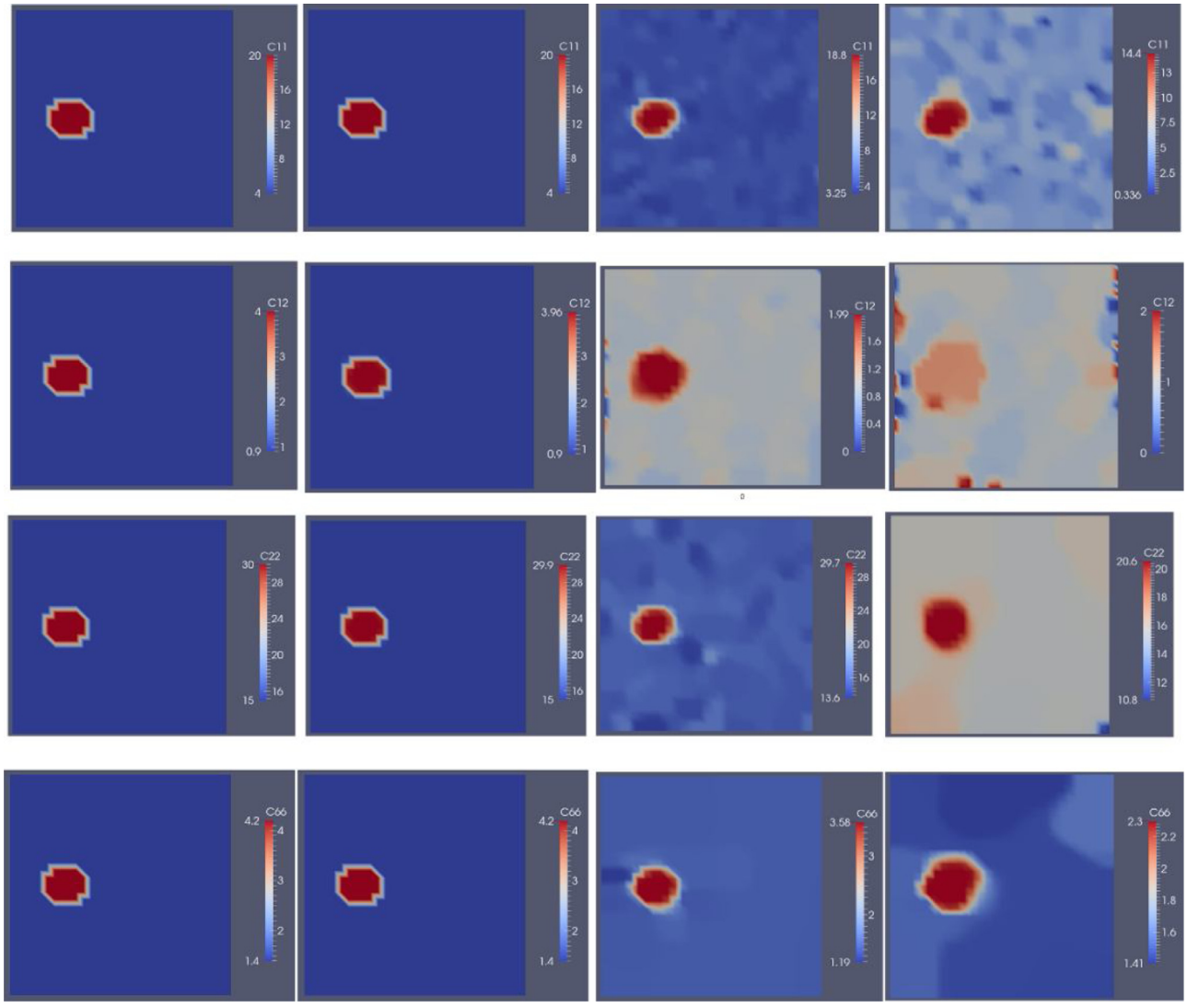

Fig. 4. Problem domain with target material parameter distributions C_{11},C_{12},C_{22},C_{66} are defined in the first column and presented from top row to bottom row, respectively. Column 2 to Column 4 represent parameter reconstructions using 6 displacement measurements with 0%, 1%, and 3% noise, respectively. (Unit in the color bar: 10KPa).

4 are associated with noise levels of 0%, 1%, and 3%, respectively. The regularization factor for each mechanical parameter is listed in Table 2. We observe that the recovered orthotropic linear elastic parameter distributions for the noise free case (second column in Fig. 3) are fairly close to the target distributions (first column in Fig. 3). Furthermore, for 1% noise, all parameter distributions except for C_{12} are well-recovered with respect to shape of the inclusions and its overall quantitative reconstruction. For the C_{12} parameter, the shape of the inclusion becomes larger and its value in the inclusion is significantly smaller than the target. For 3% noise (fourth column in Fig. 3, the inclusion shape for all parameter distributions except for C_{12} are visible (though distorted), but the overall quantitative reconstructions of all mechanical parameters are of poor quality and significantly lower than their target distributions. Next, we include two additional displacement measurements from biaxial testing in Fig. 2 (e) and (f), thus have a total of 6 displacement fields to reconstruct the mechanical parameters, shown in Fig. 4. The corresponding regularization factors are listed in Table 3. For a low noise level, the orthotropic elastic parameter distribution can be well recovered quantitatively, similar to what we observed in Fig. 3, while they are poorly recovered at a higher noise level. We also observe that for 3% noise, the inclusion shape and parameter values in the mapped distribution of the parameter C_{12} can be improved after including displacement fields from biaxial tests and thereby increasing the total number of displacement measurements.

So far we have shown that the reconstructions are fairly reasonable even in the presence of noise for a single stiff inclusion. Since the

Table 2
Regularization factors associated with computations in Fig. 3.

	C_{11}	C_{12}	C_{22}	C_{66}
0% noise	10^{-12}	10^{-12}	10^{-12}	10^{-12}
1% noise	5.0×10^{-10}	2.0×10^{-10}	1.0×10^{-10}	2.0×10^{-10}
3% noise	3.0×10^{-9}	5.0×10^{-10}	2.0×10^{-10}	2.0×10^{-9}

Table 3
Regularization factors associated with computations in Fig. 4.

	C_{11}	C_{12}	C_{22}	C_{66}
0% noise	10^{-12}	10^{-12}	10^{-12}	10^{-12}
1% noise	3.0×10^{-10}	5.0×10^{-11}	2.0×10^{-11}	3.0×10^{-10}
3% noise	1.0×10^{-9}	2.0×10^{-10}	3.0×10^{-10}	2.0×10^{-9}

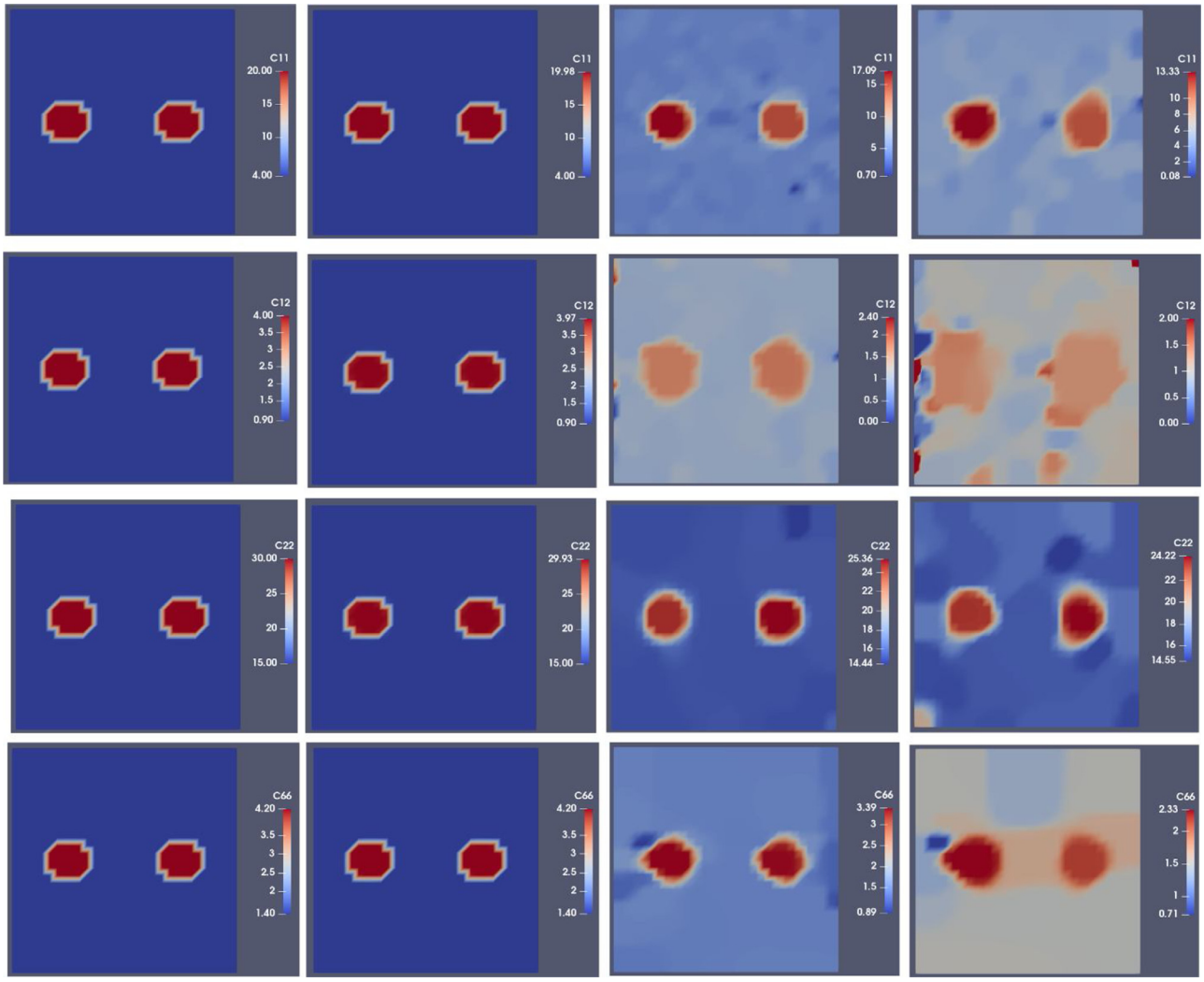

Fig. 5. Problem domain with target material parameter distributions C_{11},C_{12},C_{22},C_{66} are defined in the first column and presented from top row to bottom row, respectively. Column 2 to Column 4 represent parameter reconstructions using 4 displacement measurements with 0%, 1%, and 3% noise, respectively. (Unit in the color bar: 10KPa).

orthotropic elastic parameters are specified as unknowns on finite element mesh nodes and no assumptions are made on the presence of any stiff regions, it should be possible to recover additional non-homogeneities. To demonstrate this, we define a second stiff inclusion with the same orthotropic elastic parameters as in the previous examples, with target domain given in the first column of Fig. 5 for the orthotropic elastic parameters C_{11}, C_{12}, C_{22}, C_{66} from row 1 to 4, respectively. The reconstructions with 4 displacement fields are given in Fig. 5 in columns 2, 3, and 4 for noise levels of 0%, 1%, and 3%. The associated regularization factors are listed in Table 4. We observe that the reconstructions behave similar to the reconstructions obtained with 1 inclusion.

For some materials, the angle of material axes with the reference coordinate system (here also referred to as “angle”) may not be known, e.g., skin tissue or engineered materials with unknown manufacturing details. Thus, in the following, we will demonstrate feasibility to recover the distribution of the angle θ in addition to the material parameters. We define the problem domain similar to the previous example with the same target material parameter distributions, but vary the angle of the material axes in the inclusion according to Table 5. As detailed for the previous examples, we create displacement fields by solving boundary value problems for given boundary conditions in Fig. 2 and augment the resulting displacement fields with noise to represent noise in displacement measurements. We also utilize the same strategy to solve the inverse problem, but now include the angle of material axes as an additional unknown. Figs. 6 and 7 present reconstructions of the mechanical property distributions using 4 and 6 full-field displacement measurements, respectively, with noise levels of 0%, 1%, and 3%. The associated regularization factors are listed in Tables 6 and 7. For no or low noise levels of 1%, the mechanical property distributions are generally well

Table 4
Regularization factors associated with computations in Fig. 5.

	C_{11}	C_{12}	C_{22}	C_{66}
0% noise	10^{-12}	10^{-12}	10^{-12}	10^{-12}
1% noise	5.0×10^{-10}	1.0×10^{-10}	1.0×10^{-10}	4.0×10^{-10}
3% noise	3.0×10^{-9}	4.0×10^{-10}	2.0×10^{-10}	3.0×10^{-9}

Table 5
Target orthotropic linear elastic material parameters used in Fig. 6.

	C_{11}(kPa)	C_{12}(kPa)	C_{22}(kPa)	C_{66}(kPa)	$\theta(^\circ)$
background	40	9	150	14	0
inclusion	200	40	300	42	30

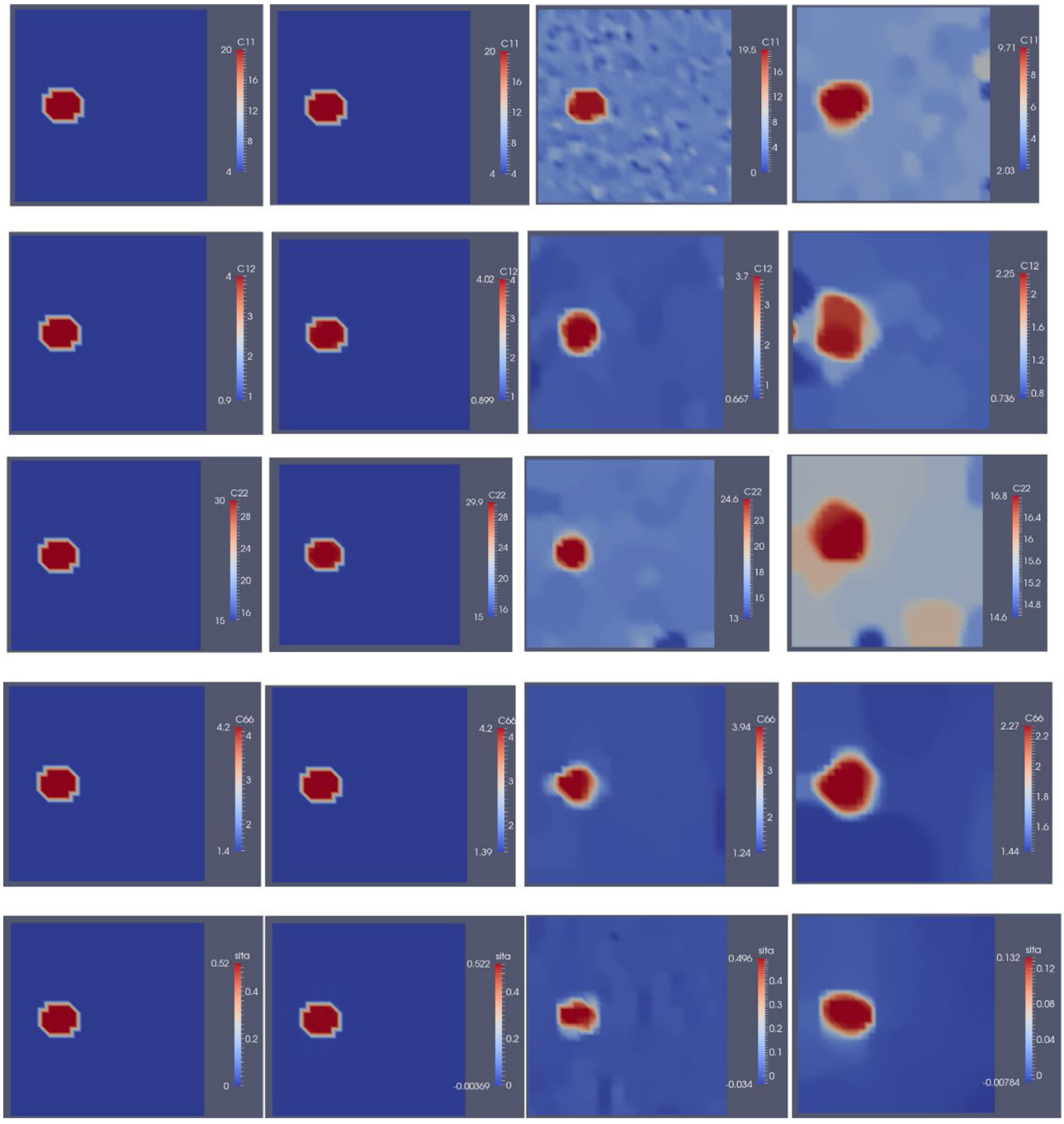

Fig. 6. Problem domain with target material parameter and angle distributions C_{11},C_{12},C_{22},C_{66}, θ are defined in the first column and presented from top row to bottom row, respectively. Column 2 to column 4 represent reconstructions using 4 displacement measurements with 0%, 1%, and 3% noise, respectively. Note that the unit of the angle θ used in the last row is in radians, and for other parameters, the unit is 10 KPa.

recovered, whereas the reconstruction of θ for 1% noise yields a slightly deteriorated inclusion shape, but overall quantitative values in inclusion and background are well reconstructed. For higher noise levels of 3%, the mechanical property distribution and angle are poorly reconstructed. More precisely, the shape of the inclusion appears enlarged, and the mechanical property values overall are underestimated.

Table 6
Regularization factors associated with computations in Fig. 6.

	C_{11}	C_{12}	C_{22}	C_{66}	θ
0% noise	10^{-12}	10^{-12}	10^{-12}	10^{-12}	10^{-12}
1% noise	1.0×10^{-10}	8.0×10^{-11}	5.0×10^{-11}	3.0×10^{-10}	9.0×10^{-10}
3% noise	5.0×10^{-9}	1.0×10^{-9}	4.0×10^{-10}	4.0×10^{-9}	2.5×10^{-8}

Table 7
Regularization factors associated with computations in Fig. 7.

	C_{11}	C_{12}	C_{22}	C_{66}	θ
0% noise	10^{-12}	10^{-12}	10^{-12}	10^{-12}	10^{-12}
1% noise	1.0×10^{-10}	8.0×10^{-11}	5.0×10^{-11}	3.0×10^{-10}	1.0×10^{-9}
3% noise	2.0×10^{-9}	4.0×10^{-10}	2.0×10^{-10}	2.0×10^{-9}	3.0×10^{-8}

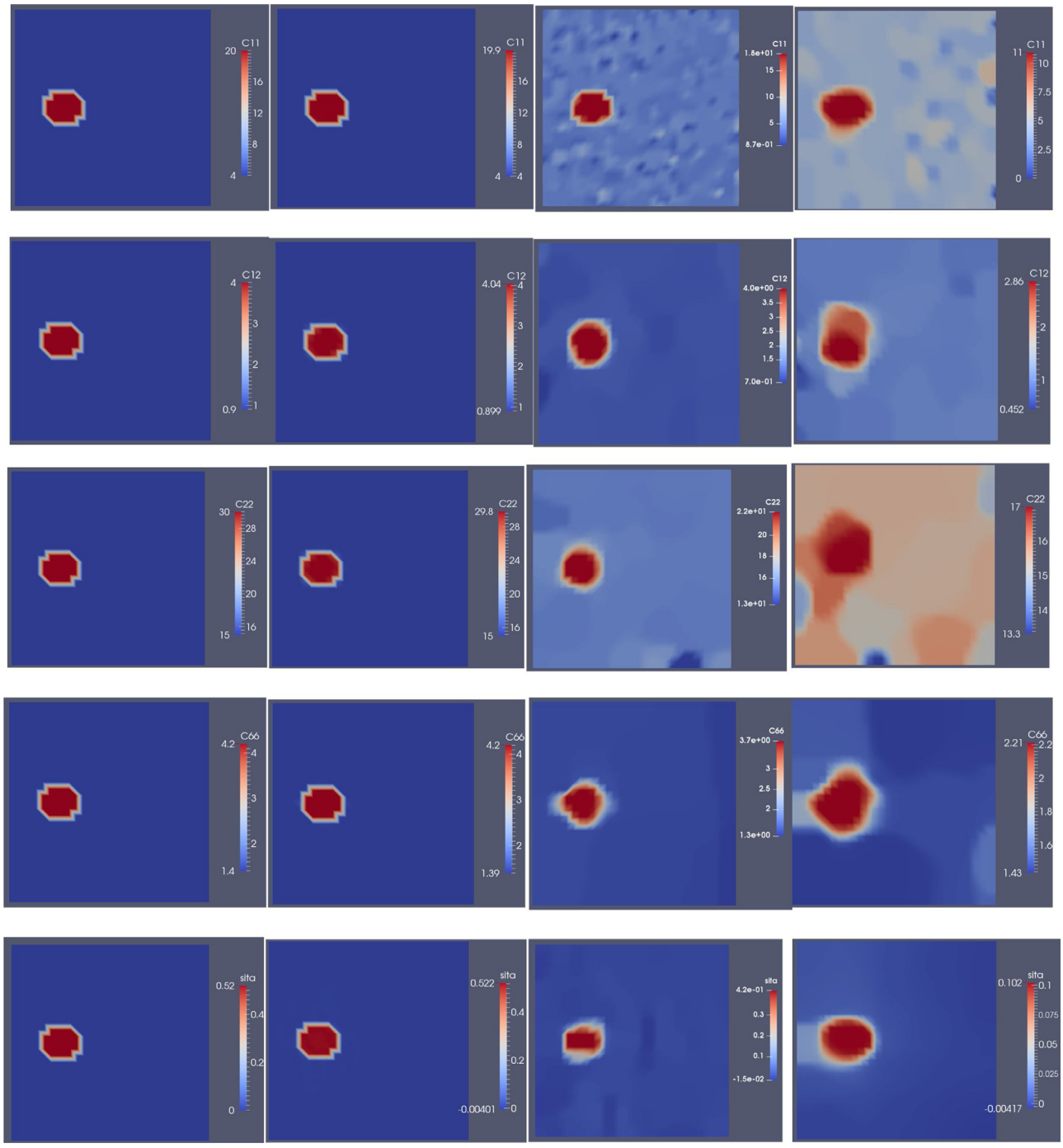

Fig. 7. Problem domain with target material parameter and angle distributions C_{11},C_{12},C_{22},C_{66}, θ are defined in the first column and presented from top row to bottom row, respectively. Column 2 to Column 4 represent reconstructions using 6 displacement measurements with 0%, 1%, and 3% noise, respectively. Note that the unit of rotation θ used in the last row is in radians, and for other parameters, the unit is 10KPa.

3.2. Reconstructions using L-1 regularization

In the following, we explore the performance of reconstructing the orthotropic elastic parameter distributions using the L-1 regularization, defined in the second row in Eq. (6). Fig. 8 shows the reconstructions of the orthotropic elastic parameters C_{11}, C_{12}, C_{22}, C_{66} in rows 1, 2, 3, and 4, respectively. Columns 2, 3, and 4 represent reconstructions with noise levels of 0%, 1%, and 3%, respectively. The regularization factors associated with these reconstructions are given in Table 8. We observe that the reconstructions with 1% and 3% noise are very poor and the solutions oscillate extremely throughout the entire domain.

Table 8
Regularization factors associated with computations in Fig. 8.

	C_{11}	C_{12}	C_{22}	C_{66}
0% noise	10^{-12}	10^{-12}	10^{-12}	10^{-12}
1% noise	2.0×10^{-8}	5.0×10^{-9}	3.0×10^{-9}	9.0×10^{-9}
3% noise	1.0×10^{-7}	9.0×10^{-9}	7.0×10^{-9}	7.0×10^{-8}

3.3. Reconstructions using L-2 regularization

Next, we explore the performance of reconstructing the orthotropic elastic parameter distributions using the L-2 regularization, defined in

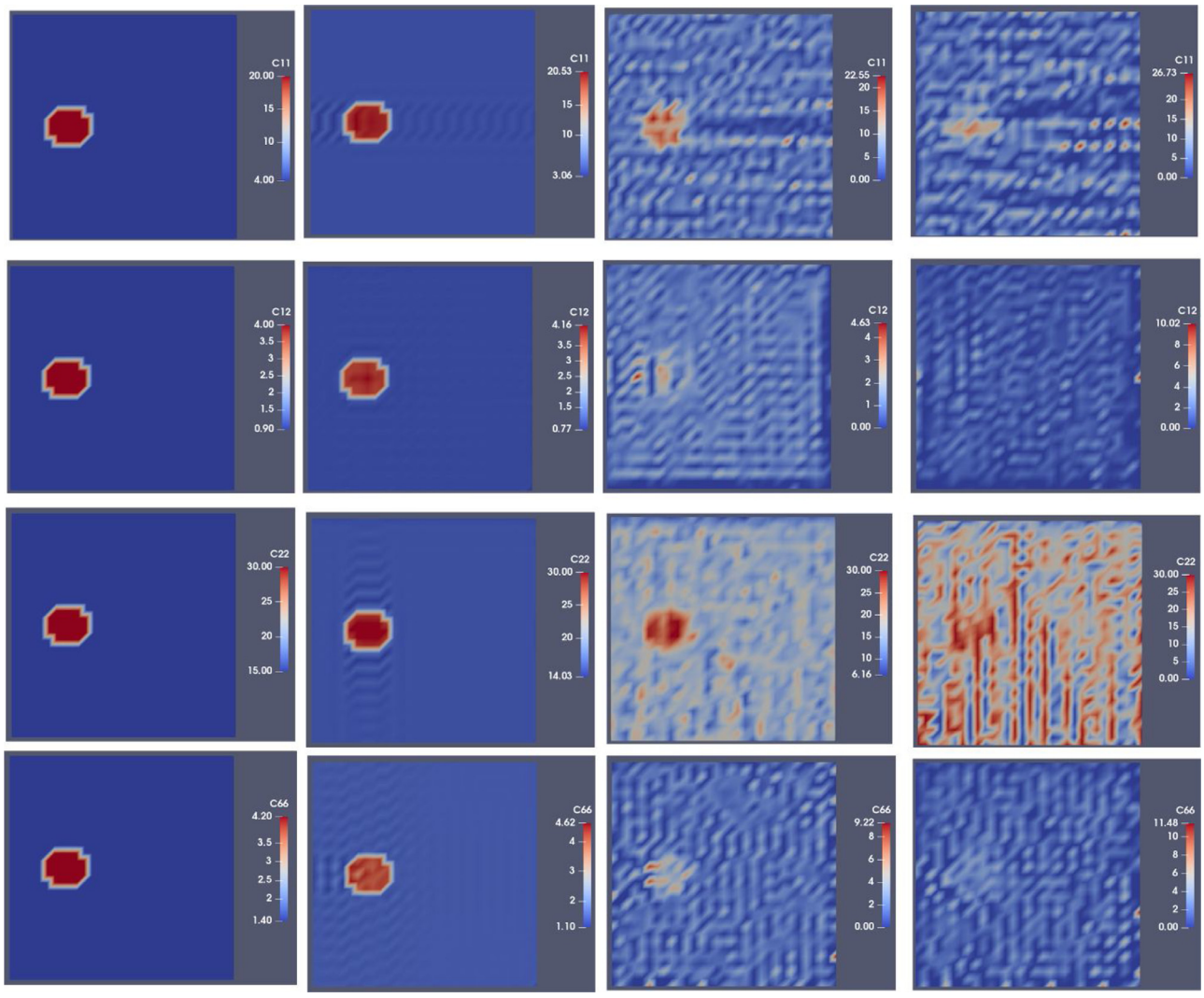

Fig. 8. Problem domain with target material parameter distributions C_{11},C_{12},C_{22},C_{66} are defined in the first column and presented from top row to bottom row, respectively. Column 2 to Column 4 represent parameter reconstructions using 4 displacement measurements with 0%, 1%, and 3% noise, respectively. (Unit in the color bar: 10KPa).

Table 9
Regularization factors associated with computations in Fig. 9.

	C_{11}	C_{12}	C_{22}	C_{66}
0% noise	10^{-12}	10^{-12}	10^{-12}	10^{-12}
1% noise	7.0×10^{-9}	1.0×10^{-8}	8.0×10^{-10}	2.0×10^{-8}
3% noise	8.0×10^{-9}	1.0×10^{-9}	5.0×10^{-9}	6.0×10^{-9}

Table 10
Regularization factors associated with computations in Fig. 10. (We use the same regularization factors for TVD part and L-1 part).

	C_{11}	C_{12}	C_{22}	C_{66}
0% noise	10^{-12}	10^{-12}	10^{-12}	10^{-12}
1% noise	5.0×10^{-10}	2.0×10^{-10}	1.0×10^{-10}	2.0×10^{-10}
3% noise	3.0×10^{-9}	5.0×10^{-10}	2.0×10^{-10}	2.0×10^{-9}

the third row in Eq. (6). Fig. 9 shows the reconstructions of the orthotropic elastic parameters C_{11}, C_{12}, C_{22}, C_{66} in rows 1, 2, 3, and 4, respectively. Column 2, 3, and 4 represent reconstructions with noise levels of 0%, 1%, and 3%, respectively. The regularization factors associated with these reconstructions are given in Table 9. We observe that the reconstructions with 1% and 3% noise are very poor and the solutions oscillate extremely throughout the entire domain.

3.4. Reconstructions using compound regularization

Finally, we test the performance of reconstructing the orthotropic elastic parameter distributions using the compound regularization. Fig. 10 shows the reconstructions of the orthotropic elastic parameters C_{11}, C_{12}, C_{22}, C_{66} in rows 1 to 4, respectively. Columns 2, 3, and 4 represent reconstructions with noise levels of 0%, 1%, and 3%, respectively. The regularization factors associated with these reconstructions are given in Table 10. We observe that the reconstructions of C_{22} with 3% noise are very poor and the solutions oscillate extremely throughout the entire domain. For other mechanical properties, the reconstruction results look decent.

3.5. Theoretical analysis

We observed from the reconstructions in this paper that C_{12} was poorly recovered. To understand why this happens, we employ a 2-D homogeneous and orthotropic square membrane with unit length of 1 on each side and subjected to biaxial testing as shown in Fig. 11. We

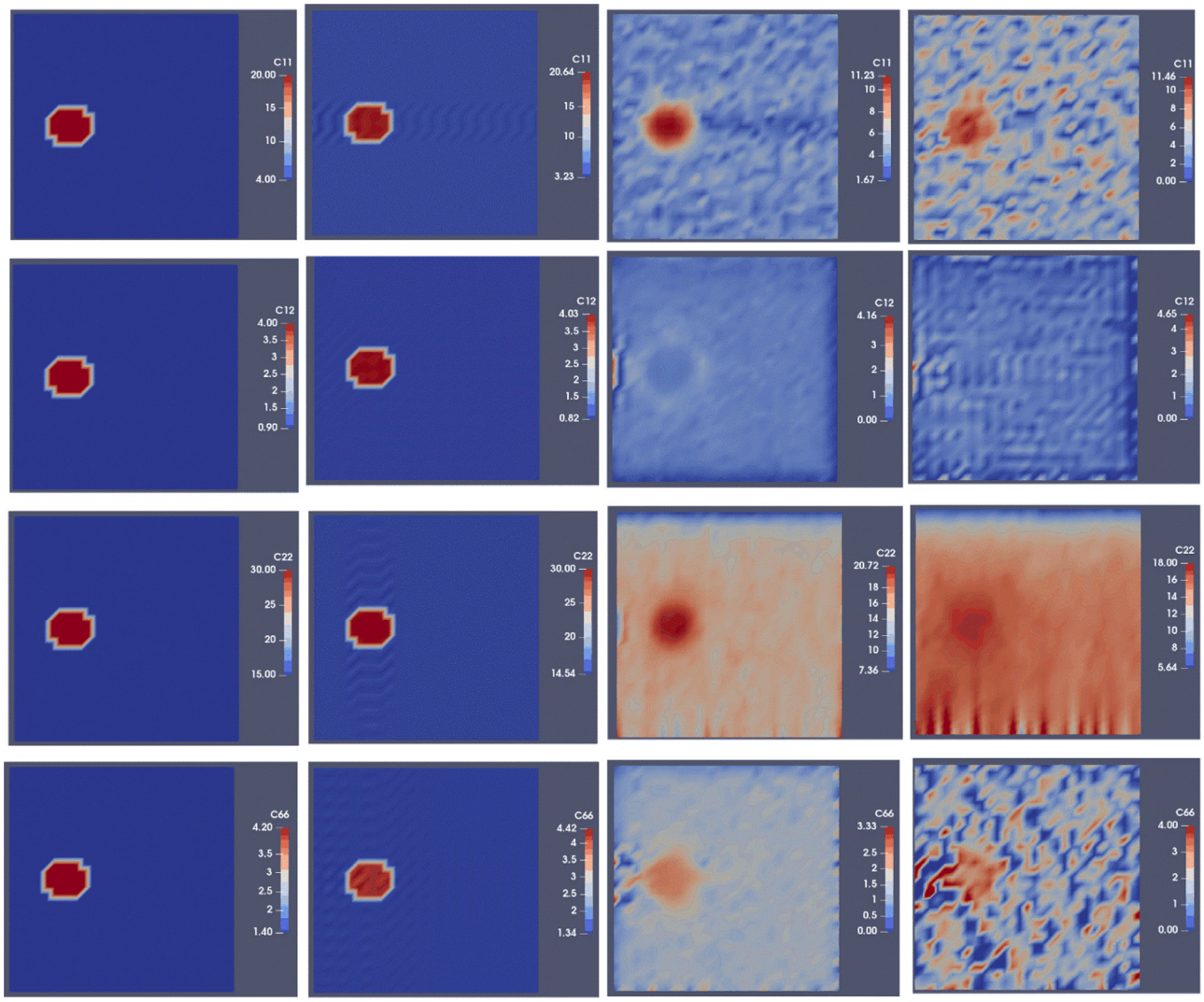

Fig. 9. Problem domain with target material parameter distributions C_{11},C_{12},C_{22},C_{66} are defined in the first column and presented from top row to bottom row, respectively. Column 2 to Column 4 represent parameter reconstructions using 4 displacement measurements with 0%, 1%, and 3% noise, respectively. (Unit in the color bar: 10KPa).

assume that the material axis is aligned with x-y (reference) plane, thus we only consider the three parameters C_{11}, C_{22} and C_{12} for the analysis. Since the solution of the inverse problem relies on a gradient based optimization approach, the gradient of the objective function with respect to the optimization variables may help to understand the performance of the optimization scheme and the results presented in this paper. Thus, in the following analysis, we will derive the analytical solution for the gradient of the objective function with respect to β_j. Let us also assume that there is no noise in measured displacements and neglect the regularization term, leading to the following objective function:

$$F = \frac{1}{2}\int_0^1 \int_0^1 \left(\left(u_x^c - u_x^m\right)^2 + \left(u_y^c - u_y^m\right)^2 \right) dxdy \tag{13}$$

where subscripts x and y denote the associated displacement components in x and y direction, respectively. As the strain fields are homogeneous throughout the domain, Eq. (5) can be expressed in terms of the strain components:

$$F = \frac{1}{6}\left(\left(\varepsilon_{xx}^c - \varepsilon_{xx}^m\right)^2 + \left(\varepsilon_{yy}^c - \varepsilon_{yy}^m\right)^2 \right) \tag{14}$$

Here, the measured strain fields ε_{xx}^m and ε_{yy}^m are determined using the target mechanical properties defined for the inclusion material in Table 1 and the applied traction defined in Fig. 2**(e)** or 2**(f)**, related by

$$\begin{Bmatrix} \varepsilon_{xx}^m \\ \varepsilon_{yy}^m \end{Bmatrix} = \begin{bmatrix} \bar{C}_{11} & \bar{C}_{12} \\ \bar{C}_{12} & \bar{C}_{22} \end{bmatrix}^{-1} \begin{Bmatrix} t_x \\ t_y \end{Bmatrix} \tag{15}$$

where $\bar{C}_{11}, \bar{C}_{12}, \bar{C}_{22}$ denote the target mechanical properties. Further, the computed strain fields ε_{xx}^c and ε_{yy}^c are given by:

$$\begin{Bmatrix} \varepsilon_{xx}^c \\ \varepsilon_{yy}^c \end{Bmatrix} = \begin{bmatrix} C_{11} & C_{12} \\ C_{12} & C_{22} \end{bmatrix}^{-1} \begin{Bmatrix} t_x \\ t_y \end{Bmatrix} \tag{16}$$

Thus, the gradient of the objective function with respect to the mechanical properties are given by

$$\frac{\partial F}{\partial \beta_j} = \frac{1}{3}\left(\left(\varepsilon_x^c - \varepsilon_x^m\right)\frac{\partial \varepsilon_x^c}{\partial \beta_j} + \left(\varepsilon_y^c - \varepsilon_y^m\right)\frac{\partial \varepsilon_y^c}{\partial \beta_j} \right) \tag{17}$$

Thus, for each parameter, the corresponding gradient is a function of C_{11},C_{12},C_{22} if the target parameter $\bar{C}_{11}, \bar{C}_{12}, \bar{C}_{22}$ are fixed. However, it is not easy to visualize 3D contour plots and draw any conclusion from them. To this end, when we calculate and plot the gradient of the objective function with respect to one mechanical property, we simplify this analysis and fixed the other two parameters to be the target. For instance, if we calculate $\partial F/\partial C_{11}$, we fix the other two parameters: C_{12} =

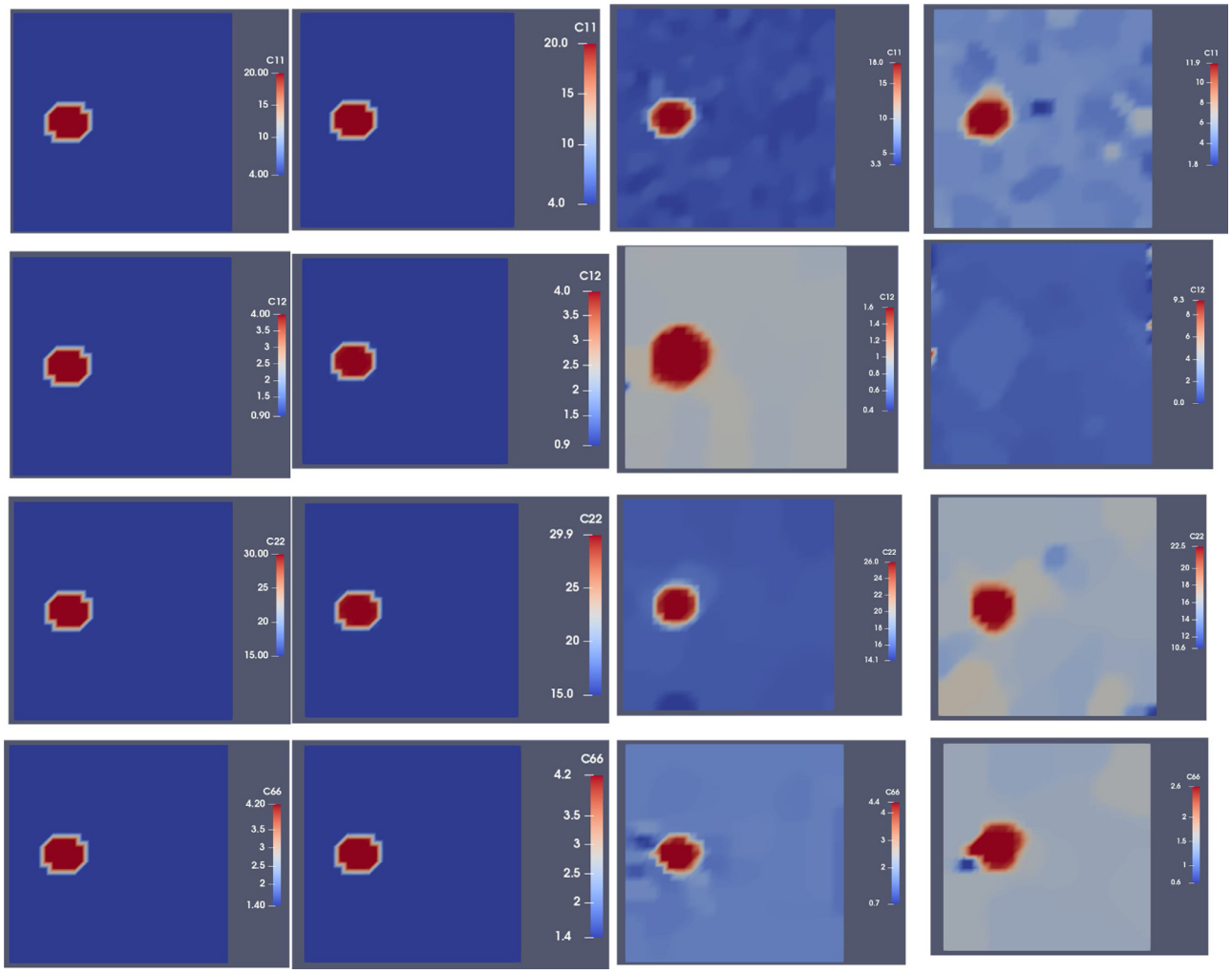

Fig. 10. Problem domain with target material parameter distributions C_{11},C_{12},C_{22},C_{66} are defined in the first column and presented from top row to bottom row, respectively. Column 2 to Column 4 represent parameter reconstructions using 4 displacement measurements with 0%, 1%, and 3% noise, respectively. (Unit in the color bar: 10KPa).

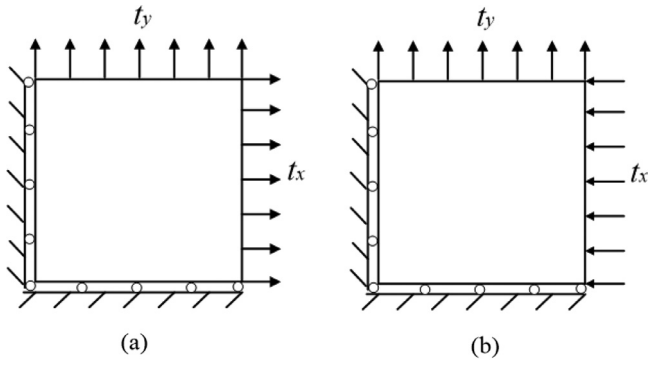

Fig. 11. A homogeneous square sample subjected to biaxial testing (a) the square sample is stretched along both directions; (b) the square sample is compressed and stretched along x and y directions, respectively.

$\bar{C}_{12}$ and $C_{22} = \bar{C}_{22}$. Thereby, Eq (17) can be rewritten as:

$$\begin{Bmatrix} \varepsilon^c_{xx} \\ \varepsilon^c_{yy} \end{Bmatrix} = \begin{bmatrix} C_{11} & \bar{C}_{12} \\ \bar{C}_{12} & \bar{C}_{22} \end{bmatrix}^{-1} \begin{Bmatrix} t_x \\ t_y \end{Bmatrix} \tag{18}$$

From Fig. 12, we observe that $\partial F/\partial C_{12}$ is much smaller than $\partial F/\partial C_{11}$ and $\partial F/\partial C_{22}$, and the mapped distribution of C_{12} may be more sensitive to noise. This may explain why the parameter C_{12} has been poorly recovered in the numerical simulations.

4. Discussion

In this work, we have shown that it is feasible to quantitatively identify the heterogeneous parameter distributions for a 2-D orthotropic linear elastic solid together with the distribution of the angle of material axes using a gradient based optimization scheme.

We tested the performance of the inverse algorithms with theoretical displacement fields acquired by solving boundary value problems with defined target non-homogenous mechanical property and angle of material axes distributions. These boundary value problems were chosen as to represent uniaxial, shear, and biaxial tests. The results using total variation diminishing regularization revealed that the orthotropic linear elastic parameter and angle distributions are sensitive to noisy data. When the noise level was low, e.g. 1% or less, the orthotropic linear elastic parameter and angle distributions were mapped well, while in the presence of a high noise level of 3% the quality of the reconstructions deteriorated significantly. The high sensitivity of the reconstructed anisotropic linear elastic parameter distributions to noise in displacement fields has also been observed in other works [38,39] with noise levels of about 0.1% to 1%. In contrast, past works using an isotropic

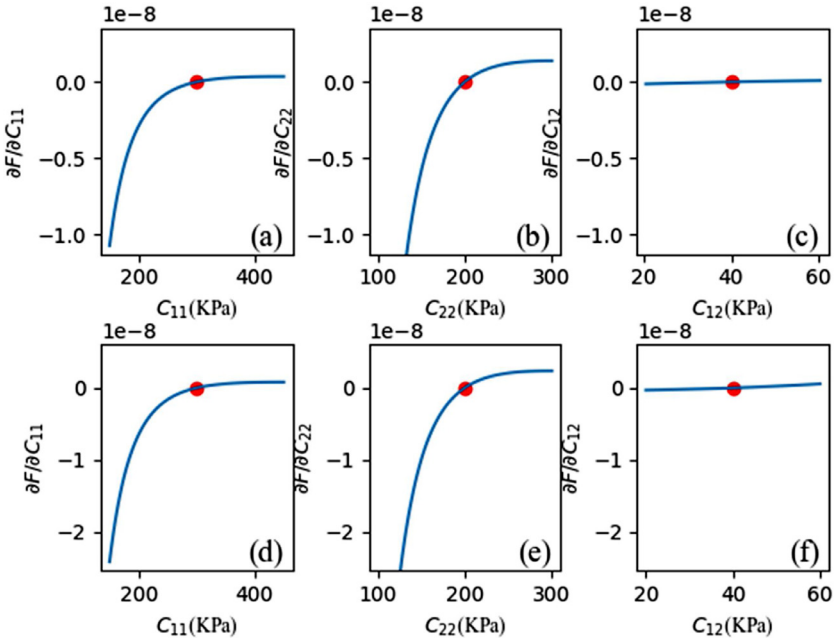

Fig. 12. Plots of the gradient of the objective function with respect to a range of elastic parameter values for different cases: Row 1 and 2 correspond to Figure 11(a) and (b), respectively. The target values are the target values used in the inclusion listed in Table 1. The red point represents the associated gradient equals zero. (For interpretation of the references to color in this figure legend, the reader is referred to the web version of this article.)

linear elastic solid yielded superior and highly accurate reconstructions in the presence of high noise levels of about 3%.

A direct comparison in performance between the work by Shore et al. [39] and this work is not possible due to two main reasons. First, their work has been done in three-dimensional space utilizing a transversely isotropic model, while our work is in two-dimensional space. Second, we map the unknown orientation of the material axes in addition to the elastic properties, while Shore et al. assumes that the material axes is known. The work by Guchhait et al. [38] utilized an orthotropic material model in two dimensional space and their results were more sensitive to noise than the reconstructions presented in this paper. In particular, the results in this paper with total variation diminishing (TVD) regularization smooth out oscillations in the reconstructions without penalizing and smoothing sharp gradients in the parameter distributions. However, we also note that the results in Guchhait et al. [38,53] were tested on problem domains with many inclusions in a homogeneous background, while our problems had at most two inclusions. Given that the reconstructions with one inclusion versus two inclusions in this paper did not make a significant difference, it is assumed that additional inclusions will not deteriorate the reconstructions much. However, the inclusions in Guchhait et al. [38] were smaller than the inclusions modeled in this paper.

We observed that uniqueness of the problem improves by including additional measured displacement fields (see Figs. 3 and 4). These additional displacement measurements need to be distinct from one another. If one were to use a measured displacement field that is off by some constant factor from another one, it would not help to steer the solution to a unique one, given that the problem is linear elastic. The only help it would provide may be some robustness towards reducing the effect of noisy measurements on the reconstructions.

Finally, we also tested L-1 regularization and L-2 regularization and observed that they do not perform well. However, compound regularization which contains the TVD regularization part performs well. Clearly, total variation diminishing regularization performs superior to L-1 and L-2 regularization in this work.

5. Conclusions

In this paper, we have presented an approach to quantitatively map the 2-D heterogeneous, orthotropic, linear elastic material parameter distributions of solids. The feasibility of this approach has been tested and it has been shown that multiple datasets are needed to uniquely reconstruct the parameter distributions. We have observed that the mapped anisotropic elastic parameter distributions are well recovered at low noise levels, while the reconstructions degrade at higher noise levels of about 3%. This preliminary study has been conducted using theoretical data with added noise to simulate noisy measurements. Future work will focus on a proof of concept with experimental datasets and generalizing this approach to three-dimensional problem domains.

Acknowledgments

The authors would like to thank the National Science Foundation under Grant No. CMMI #1663435 for partial funding of this project. Yue Mei acknowledges the support from the Fundamental Research Funds for the Central Universities (Grant No. DUT19RC(3)017). The authors would also like to thank the High Performance Research Computing at Texas A&M University for their computing resources.

References

[1] Budynas R, Nisbett K. Shigley's mechanical engineering design 9th edition. New York: McGraw-Hill Science/Engineering/Math; 2012.
[2] Freed, A.D.*Soft solids*. modeling and simulation in science, engineering and technology (Birkhäuser, basel, 2014), a primer to the theoretical mechanics of materials. 2014, New York: Springer Science & Business Media.
[3] McCullough KY, Fleck NA, Ashby MF. Uniaxial stress–strain behaviour of aluminium alloy foams. Acta Mater 1999;47(8):2323–30.
[4] Tsui T, Oliver W, Pharr G. Influences of stress on the measurement of mechanical properties using nanoindentation: part I. experimental studies in an aluminum alloy. J Mater Res 1996;11(03):752–9.
[5] Attard M, Setunge S. Stress-strain relationship of confined and unconfined concrete. Mater J 1996;93(5):432–7442.
[6] Ottosen NS. Constitutive model for short-time loading of concrete. J Eng Mech Div ASCE 1979;105:127–41.
[7] Kiser M, He M, Zok F. The mechanical response of ceramic microballoon reinforced aluminum matrix composites under compressive loading. Acta Mater 1999;47(9):2685–94.
[8] Wertheim MG. MÉmoire sur 1′BlasticitB et la cohesion des principaux tissues du corps humain. Annales de Chimie et de Physique 1847;21:385–414.
[9] Trowbridge E, Black M, Daniel C. The mechanical response of glutaraldehyde-fixed bovine pericardium to uniaxial load. J Mater Sci 1985;20(1):114–40.
[10] Fung Y. Elasticity of soft tissues in simple elongation. Am J Physiol 1967;213(6):1532–44.
[11] Mousavi SR, Rivaz H, Czarnota GJ, Samani A, Sadeghi-Naini A. Ultrasound elastography of the prostate using an unconstrained modulus reconstruction technique: a pilot clinical study. Transl Oncol 2017;10(5):744–51.

[12] Goenezen S, Dord JF, Sink Z, Barbone P, Jiang J, Hall TJ, Oberai AA. Linear and nonlinear elastic modulus imaging: an application to breast cancer diagnosis. Med Imaging, IEEE Trans 2012;31(8):1628–37.
[13] Jiang J, Peng B. A normalized shear deformation indicator for ultrasound strain elastography in breast tissues: an in vivo feasibility study. BioMed Res Int 2018;2018.
[14] Wittek A, Derwich W, Karatolios K, Fritzen CP, Vogt S, Schmitz-Rixen T, Blase C. A finite element updating approach for identification of the anisotropic hyperelastic properties of normal and diseased aortic walls from 4D ultrasound strain imaging. J Mech Behav Biomed Mater 2016;58:122–38.
[15] Smyl D, Bossuyt S, Liu D. OpenQSEI: a matlab package for quasi static elasticity imaging. SoftwareX 2019;9:73–6.
[16] Wiskin JW, Borup DT, Iuanow E, Klock J, Lenox MW. 3-D nonlinear acoustic inverse scattering: algorithm and quantitative results. IEEE Trans Ultrasonics, Ferroelectrics Frequency Control 2017;64(8):1161–74.
[17] Yamakoshi Y, Sato J, Sato T. Ultrasonic imaging of internal vibration of soft tissue under forced vibration. IEEE Trans Ultrason Ferroelectr Freq Control 1990;37(2):45–53.
[18] Krouskop TA, Dougherty DR, Vinson FS. A pulsed doppler ultrasonic system for making noninvasive measurements of the mechanical properties of soft tissue. J Rehabil Res Dev 1987;24(2):1–8.
[19] Mei Y, Goenezen S. Mapping the viscoelastic behavior of soft solids from time harmonic motion. J Appl Mech 2018;85(4) p. 041003-041003-11.
[20] Freimann FB, Muller S, Streitberger KJ, Guo J, Rot S, Ghori A, Vajkoczy P, Reiter R, Sack I, Braun J. MR elastography in a murine stroke model reveals correlation of macroscopic viscoelastic properties of the brain with neuronal density. NMR Biomed 2013;26(11):1534–9.
[21] Sinkus R, Tanter M, Catheline S, Lorenzen J, Kuhl C, Sondermann E, Fink M. Imaging anisotropic and viscous properties of breast tissue by magnetic resonance-elastography. Magn Reson Med 2005;53:372–87.
[22] Van Houten EEW, Doyle MM, Kennedy FE, Weaver JB, Paulsen KD. Initial in vivo experience with steady-state subzone-based mr elastography of the human breast. J Magn Reson Imaging 2003;17(1):72–85.
[23] Park E, Maniatty AM. Shear modulus reconstruction in dynamic elastography: time harmonic case. Phys Med Biol 2006;51:3697–721.
[24] Midgett M, Goenezen S, Rugonyi S. Blood flow dynamics reflect degree of outflow tract banding in HH18 chicken embryos. J R Soc Interface 2014;11(100).
[25] Schmitt J. OCT elastography: imaging microscopic deformation and strain of tissue. Opt Express 1998;3(6):199–211.
[26] Dong L, Wijesinghe P, Dantuono JT, Sampson DD, Munro PRT, Kennedy BF, Oberai AA. Quantitative compression optical coherence elastography as an inverse elasticity problem. IEEE J Sel Topics Quantum Electron 2016;22(3):277–87.
[27] Qiu Y, Wang Y, Xu Y, Chandra N, Haorah J, Hubbi B, Pfister BJ, Liu X. Quantitative optical coherence elastography based on fiber-optic probe for in situ measurement of tissue mechanical properties. Biomed Optics Express 2016;7(2):688–700.
[28] Kirkpatrick SJ, Wang RK, Duncan DD. OCT-based elastography for large and small deformations. Opt Express 2006;14(24):11585–97.
[29] Larin KV, Sampson DD. Optical coherence elastography - OCT at work in tissue biomechanics. Biomed Optics Express 2017;8(2):1172–202.
[30] Bruck HA, McNeill SR, Sutton MA, Peters WH. Digital image correlation using newton-raphson method of partial differential correction. Exp Mech 1989;29(3):261–7.
[31] Sutton MA, Wolters WJ, Peters WH, Ranson WF, McNeill SR. Determination of displacements using an improved digital correlation method. Image Vision Comput 1983;1(3):133–9.
[32] Iliopoulos A, Michopoulos JG. Meshless methods for full field displacement and strain measurement. Adv Comput Inf Eng Res 2014;1:28.
[33] Mei Y, Stover B, Kazerooni NA, Srinivasa A, Hajhashemkhani M, Hematiyan M, Goenezen S. A comparative study of two constitutive models within an inverse approach to determine the spatial stiffness distribution in soft materials. Int J Mech Sci 2018;140:446–54.
[34] Avril S, Pierron F, Sutton MA, Yan J. Identification of elasto-visco-plastic parameters and characterization of luders behavior using digital image correlation and the virtual fields method. Mech Mater 2008;40(9):729–42.
[35] Gerbig D, Bower A, Savic V, Hector LG. Coupling digital image correlation and finite element analysis to determine constitutive parameters in necking tensile specimens. Int J Solids Struct 2016;97:496–509.
[36] Mei Y, Fulmer R, Raja V, Wang SC, Goenezen S. Estimating the non-homogeneous elastic modulus distribution from surface deformations. Int J Solids Struct 2016;83:73–80.
[37] Mei Y, Wang S, Shen X, Rabke S, Goenezen S. Mechanics based tomography: a preliminary feasibility study. Sensors 2017;17(5):1075.
[38] Guchhait S, Banerjee B. Anisotropic linear elastic parameter estimation using error in the constitutive equation functional. Proc R Soc Math Physical Eng Sci 2016;472(2192):20160213.
[39] Shore SW, Barbone PE, Oberai AA, Morgan EF. Transversely isotropic elasticity imaging of cancellous bone. J Biomech Eng 2011;133(6):061002.
[40] Smyl D, Antin K-N, Liu D, Bossuyt S. Coupled digital image correlation and quasi-static elasticity imaging of inhomogeneous orthotropic composite structures. Inverse Probl 2018;34(12):124005.
[41] Tsai SW, Pagano NJ. Invariant properties of composite materials.. DTIC Document; 1968.
[42] Liu, D., Kolehmainen, V., Siltanen, S., and Seppanen, A. Estimation of conductivity changes in a region of interest with electrical impedance tomography. arXiv preprint arXiv:1403.6587, 2014.
[43] Liu D, Kolehmainen V, Siltanen S, Laukkanen A-M, Seppänen A. Nonlinear difference imaging approach to three-dimensional electrical impedance tomography in the presence of geometric modeling errors. IEEE Trans Biomed Eng 2016;63(9):1956–65.
[44] Xue F, Pan H, Wu R, Liu X, Liu J. Optimization of compound regularization parameters based on stein's unbiased risk estimate. IEEE International Conference on Acoustics, Speech and Signal Processing (ICASSP); 2017.
[45] Goenezen S, Barbone P, Oberai AA. Solution of the nonlinear elasticity imaging inverse problem: the incompressible case. Comput Methods Appl Mech Eng 2011;200(13–16):1406–20.
[46] Mei Y, Kuznetsov S, Goenezen S. Reduced boundary sensitivity and improved contrast of the regularized inverse problem solution in elasticity. J Appl Mech 2016;83(3):031001.
[47] Zhu C, Byrd RH, Lu P, Nocedal J. Ll-BFGS-B: FORTRAN Subroutines for Large Scale Bound Constrained Optimization, Evanston, Illinois: EECS Department, Northwestern University; 1994. in Tech. Report, NAM-11.
[48] Zhu C, Byrd RH, Lu P, Nocedal J. Ll-BFGS-B: a limited memory FORTRAN code for solving bound constrained optimization problems in Tech, Evanston, Illinois: EECS Department, Northwestern University; 1994. Report, NAM-11.
[49] Gokhale NH, Barbone P, Oberai AA. Solution of the nonlinear elasticity imaging inverse problem: the compressible case. Inverse Prob 2008;24(4):045010.
[50] Goenezen S. Inverse problems in finite elasticity: an application to imaging the nonlinear elastic properties of soft tissues. Troy, New York: Rensselaer Polytechnic Institute; 2011.
[51] Oberai AA, Gokhale NH, Feijóo GR. Solution of inverse problems in elasticity imaging using the adjoint method. Inverse Prob 2003;19(2):297.
[52] Boyer G, Molimard J, Tkaya MB, Zahouani H, Pericoi M, Avril S. Assessment of the in-plane biomechanical properties of human skin using a finite element model updating approach combined with an optical full-field measurement on a new tensile device. J Mech Behav Biomed Mater 2013;27:273–82.
[53] Mei Y, Tajderi M, Goenezen S. Regularizing biomechanical maps for partially known material properties. Int J Appl Mech 2017;09(02):1750020.